Induction Motor Control With a Small DC-Link Capacitor Inverter Fed by Three-Phase Diode Front-end Rectifiers

SeHwan Kim, *Student Member, IEEE*, and Jul-Ki Seok, *Senior Member, IEEE*

***Abstract*—This paper presents a small film capacitor inverter-based induction motor control approach to enhance with reliability and power density of three-phase variable speed drive applications. A robust hybrid motor controller is developed to prevent performance degradation caused by the electrolytic capacitor-less inverter fed by front-end diode rectifiers. The structure of the controller combines a model-based controller (MBC) and a hexagon voltage manipulating controller (HVC). The MBC determines the command output voltage with the intersection of the torque and rotor flux linkage command. In the HVC mode, the command voltage vector is determined simply by the torque command and the hexagon-shaped inverter voltage boundary. Successful application of the control approach is corroborated by a graphical and analytical means that naturally lead to a single voltage selection rule. This paper also examines the operation sensitivity under motor parameter drifts to determine how to decouple its effect using a voltage disturbance state-filter design.**

***Index Terms*—Front-end diode rectifiers, hexagon voltage manipulating controller (HVC), model-based controller (MBC), small film capacitor inverter, three-phase variable speed drive.**

I. Introduction

In low-cost three-phase variable speed drive applications, such as heating-ventilating-air-conditioning (HVAC) systems, diode rectifiers are commonly used as the front-end circuit for nonregenerative ac–dc conversion because of their lower cost and higher reliability [1]. In these types of low-cost ac drive systems, aluminum electrolytic capacitors are commonly used to balance the difference between the instantaneous input and output power as well as suppress the voltage spikes caused by leakage inductance and switching operations, as shown in Fig. 1 [2], [3]. On the other hand, the dc-bus capacitor is not only bulky and heavy but it is also one of the least reliable components on various power electronic topologies. Furthermore, the parasitic lead inductance can cause voltage spikes, which are a major factor in the failure of power electronic devices.

A failure survey of switch mode power supplies reported that electrolytic capacitors are responsible for more than half of the breakdowns of an inverter [4]. Therefore, there is increasing interest in the monitoring lifetime of electrolytic capacitors for reliable and safe operation [4]–[7]. On the other hand, offline monitoring techniques [4], [5] require additional measurements as well as *a priori* data for the reference model, which makes monitoring process complicated and difficult. A previously reported online method [6] for estimating the capacitance cannot be applied to inverters fed by diode rectifiers.

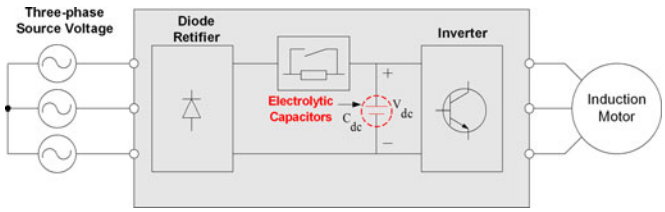

Fig. 1. Three-phase diode rectifier and PWM inverter for IM drive.

In this regard, a range of regenerative converters and control methods have been proposed in order to minimize or reduce these passive components on a dc bus. The focus of most studies has been on how to reduce the dc-bus capacitor of three-phase pulse width modulation (PWM) rectifiers and single-phase diode rectifiers [7]–[11]. All previous studies were equipped with a conventional closed-loop current controller to regulate the air-gap torque and flux linkage of ac motors. However, instantaneous current control in a small dc-bus capacitor inverter with the diode rectifier front-end is not straightforward because the dc-link voltage and output power to the motor decrease periodically due to the absence of energy storage. This rapid dc voltage reduction drives the motor to be operated frequently in the field-weakening region below a based speed. Therefore, the current control strategy becomes more complicated under voltage-limited conditions because multiple-objective subcontrollers, such as field-weakening, antiwindup control, and overmodulation scheme, should be designed carefully based on the complex tradeoff between the subcontrol actions and current control dynamics [12], [13]. Furthermore, realization of the maximum voltage utilization fails because a circular voltage limit is considered an operation boundary instead of a hexagonal limit [8].

This paper presents a position sensorless vector-controlled induction motor (IM) drive system integrated into HVAC applications. The motor power is supplied by a small dc-link film capacitor inverter fed by a three-phase diode front-end rectifier. A PI motor-current-regulator-free control strategy is proposed to meet the aforementioned challenges by combining

Manuscript received March 31, 2014; revised June 18, 2014; accepted July 28, 2014. Date of publication July 31, 2014; date of current version December 23, 2014. This work was supported by the National Research Foundation of Korea grant funded by the Korea government (MSIP) (2010-0028509). Recommended for publication by Associate Editor D. O. Neacsu.

The authors are with the School of Electrical Engineering, Yeungnam University, Gyeongbuk 712-749, Korea (e-mail: ksh8508@ynu.ac.kr; doljk@ynu.ac.kr).

Color versions of one or more of the figures in this paper are available online at http://ieeexplore.ieee.org.

Digital Object Identifier 10.1109/TPEL.2014.2344693

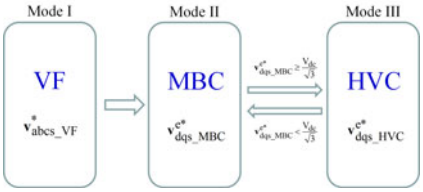

Fig. 2. Proposed IM control strategy for small capacitor inverters.

a model-based controller (MBC) and a hexagon voltage manipulating controller (HVC). The MBC finds the command output voltage with the intersection of the torque and rotor flux linkage command. In the HVC mode, the command voltage vector can be determined simply by the torque command and the hexagon voltage boundary. The MBC is performed under nonlimited conditions and motor control is handed automatically over to the proposed HVC in the voltage shortage region. These voltage selection rules allow for the choice of an objective voltage vector in the absence of PI control gains, subcontrollers, and observers for closed-loop control. The control strategy was implemented on a 1.5-kW IM drive that was equipped with a 20-μF film capacitor to confirm its feasibility.

II. Motor Controller Design With Small DC-Link Capacitor Inverter

A. Design and Analysis of a Motor Controller

Fig. 2 shows a block diagram of the proposed control strategy for an IM using a complex vector representation. Here, $\mathbf{v}^{*}_{abcs}$ and $\mathbf{v}^{e*}_{dqs}$ are the stator voltage commands in the *abc*-reference frame and the synchronous reference frame, respectively, and $V_{\rm dc}$ denotes the measured dc-link voltage. When starting (Mode I), the scalar Volts/Hz or *V/f* open-loop control is introduced to avoid the lack of observability of the motor back-EMF voltage at low speeds. This feature permits the drive system to satisfy the starting speed requirement of the back-EMF tracking-based position sensorless operation, of which the threshold begins in the vicinity of 10% of the rated speed. The control authority is then handed over to model-based control (MBC, Mode II) or hexagon voltage manipulating control (HVC, Mode III), depending on the amount of available dc-link voltage.

The motor stator voltage and flux linkage equation can be expressed using a complex vector representation:

$$\mathbf{v}^{e}_{dqs} = R_s \mathbf{i}^{e}_{dqs} + \sigma L_s \frac{d\mathbf{i}^{e}_{dqs}}{dt} + \mathbf{J}\omega_e \sigma L_s \mathbf{i}^{e}_{dqs} + \frac{L_m}{L_r}\frac{d\lambda^{e}_{dqr}}{dt} + \mathbf{J}\frac{L_m}{L_r}\omega_e \lambda^{e}_{dqr} \quad (1)$$

where $\mathbf{i}^{e}_{dqs}$ is the *d*–*q* axis stator current vector in the synchronous reference frame, $\mathbf{J} = \begin{bmatrix} 0 & -1 \\ 1 & 0 \end{bmatrix}$, R_s is the stator resistance, ω_e is the synchronous angular velocity, σL_s is the stator transient leakage inductance, and λ^{e}_{dqr} represents the *d*–*q* axis stator and rotor flux linkage vector. L_m and L_r represent the magnetizing and rotor inductance, respectively.

At the steady state, the motor air-gap torque and the rotor flux linkage of the rotor flux-oriented-controlled (RFO) IM can be expressed as

$$T_e = \frac{3}{2}\frac{P}{2}\frac{L_m}{L_r}\lambda^{e}_{dr} i^{e}_{qs} \quad (2a)$$

$$\lambda^{e}_{dr} \cong L_m i^{e}_{ds} \quad (2b)$$

where P is the number of poles.

The stator voltage equation can be also simplified as

$$v^{e}_{ds} = R_s i^{e}_{ds} - \omega_e \sigma L_s i^{e}_{qs} \quad (3a)$$

$$v^{e}_{qs} = R_s i^{e}_{qs} + \omega_e L_s i^{e}_{ds}. \quad (3b)$$

By combining (2a), (2b), (3a), and (3b), the torque and rotor flux linkage command can be obtained as a function of the rotor speed:

$$T^{*}_{e} = \frac{3}{2}\frac{P}{2}\frac{L_m}{L_r}\lambda^{e*}_{dr}\left(\frac{v^{e*}_{ds} - R_s i^{e*}_{ds}}{-\omega_e \sigma L_s}\right) \quad (4)$$

$$\lambda^{e*}_{dr} = L_m \frac{v^{e*}_{qs} - R_s i^{e*}_{qs}}{\omega_e L_s}. \quad (5)$$

Fig. 3(a) presents a graphical representation of the torque and rotor flux between (4) and (5) in the synchronously rotating *dq* volt plane. The desired torque of (4) forms a vertical line in the complex *dq* plane and is shown in blue. The rotor flux linkage line is shown in red, which is parallel to the *d*-axis.

When the voltage solutions remain within $V_{\rm dc}/\sqrt{3}$ (circular voltage boundary), which is called the MBC operation, they become feasible voltage vectors at the next sampling time. The stator voltage command $\mathbf{v}^{e*}_{dqs\_\rm MBC}$ can be obtained simply as

$$v^{e*}_{ds\_\rm MBC} = -\omega_e \sigma L_s \left(\frac{T^{*}_{e}}{\frac{3}{2}\frac{P}{2}\frac{L_m}{L_r}\lambda^{e*}_{dr}}\right) + R_s i^{e*}_{ds} \quad (6a)$$

$$v^{e*}_{qs\_\rm MBC} = \omega_e L_s \frac{\lambda^{e*}_{dr}}{L_m} + R_s i^{e*}_{qs}. \quad (6b)$$

Fig. 3(b) shows a zoomed view of the stator voltage solutions between (6a) and (6b) in the *dq* volt plane. At low speeds, the *d*-axis voltage solution $v^{e*}_{ds\_\rm MBC}$ is positive because the stator resistance drop is dominant. As ω_e increases, $v^{e*}_{ds\_\rm MBC}$ shifts to the left half-plane. On the other hand, the *q*-axis voltage solution $v^{e*}_{qs\_\rm MBC}$ of (6b) shifts downward along the *q*-axis direction as the flux decreases at a certain rotor speed or the rotor speed decreases for a given flux.

The motor speed elevation or the dc-link voltage reduction drives $\mathbf{v}^{e*}_{dqs\_\rm MBC}$ to approach $V_{\rm dc}/\sqrt{3}$. Once $\mathbf{v}^{e*}_{dqs\_\rm MBC}$ nears the circular voltage boundary, the control switches to the proposed HVC that generates the desired air-gap torque as closely as possible, while simultaneously regulating the flux linkage magnitude under a field-weakening operation.

In practice, the MBC dominates the control action at low speeds, whereas the HVC operation dominates at high speeds. In this sense, it is reasonable to assume that the stator resistance voltage drop can be negligible in the HVC mode, which does not jeopardize the motor control performance. Therefore, in the

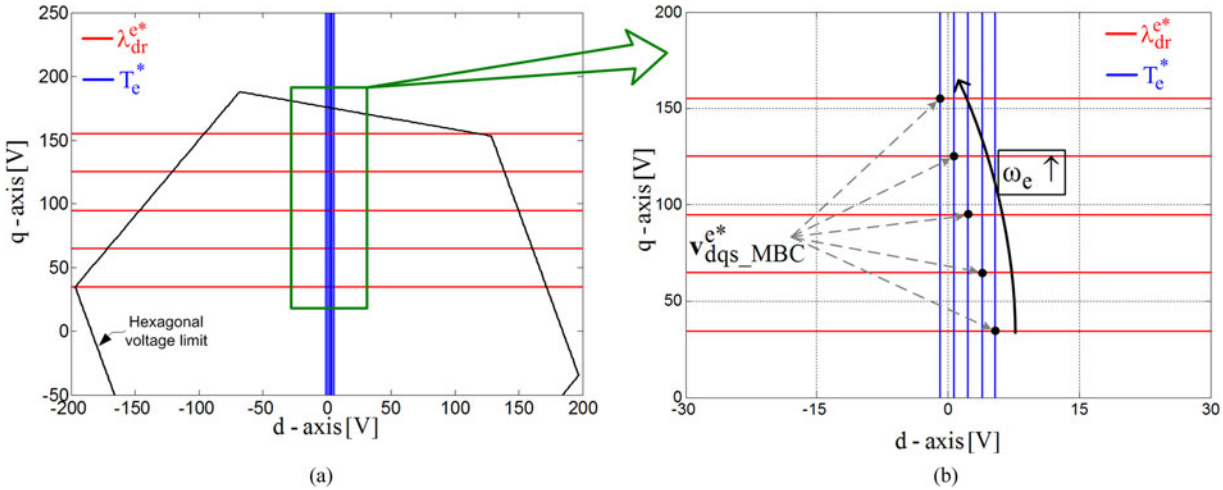

Fig. 3. Voltage command selection in the MBC mode.

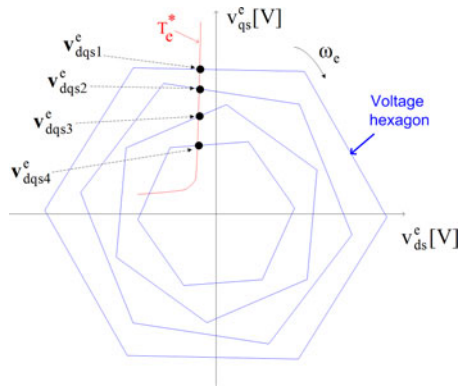

Fig. 4. Voltage command selection in the HVC mode.

HVC mode, the stator voltage equation can be simplified as

$$v_{ds}^{e*} \cong -\omega_e \sigma L_s i_{qs}^{e*}$$
$$v_{qs}^{e*} \cong \omega_e L_s i_{ds}^{e*}. \tag{7}$$

Combining (2a) and (7) provides a command torque equation with respect to the *d–q* command voltage as follows:

$$T_e^* = \frac{3}{2}\frac{P}{2}\frac{L_m^2}{L_r}\left(\frac{v_{ds}^{e*}}{-\omega_e \sigma L_s}\right)\left(\frac{v_{qs}^{e*}}{\omega_e L_s}\right) \tag{8}$$

where the torque command trajectory forms a hyperbolic curve in the *dq* volt plane.

Fig. 4 gives a schematic representation of the stator voltage solutions between the torque curves and rotating hexagon, which shrinks with the inverter dc-bus voltage. In the proposed HVC method, the intersection (marked as a black dot) of the torque line and the shrinking hexagon becomes the command voltage vector at the next sampling instant. The boundary of each rotating hexagon sector can be modeled as a straight line in the *dq* volt plane as follows [12]:

$$v_{qs}^{e}(k) = M_n\, v_{ds}^{e}(k) + B_n \tag{9}$$

where M_n and B_n are constant values given by the boundary of each hexagon sector.

The corresponding hexagon boundary (shown in blue) and the torque command curve of (9) can provide two possible stator voltage solutions that produce the desired output torque, as shown in Fig. 5. Here, the command voltage vector $\mathbf{v}_{dqs}^{e*}$ is chosen as a feasible solution because it is the only voltage to satisfy the desired stator flux magnitude. A selected voltage vector at the intersection can be uniquely expressed as

$$v_{ds\_\mathrm{HVC}}^{e*} = \frac{-B_n + \sqrt{B_n^2 - 4M_n\gamma}}{2M_n} \tag{10a}$$
$$v_{qs\_\mathrm{HVC}}^{e*} = M_n \cdot v_{ds\_\mathrm{HVC}}^{e*} + B_n \tag{10b}$$

where $\gamma = \frac{T_e^*}{\frac{3}{2}\frac{P}{2}\frac{L_m^2}{L_r}\frac{1}{\omega_e^2 L_s \sigma L_s}}$. Using this algorithm, the motor torque is regulated around a desired torque line in the presence of rapid voltage variations.

How the HVC performs the field-weakening operation during the inverter voltage reduction period should be investigated. As shown in Fig. 4, the possible voltage solutions for a given command torque trajectory are determined on the rotating hexagon with the dc-link voltage fluctuation. The voltage solution naturally moves to a downward q-axis direction (from $\mathbf{v}_{dqs1}^{e}$ to $\mathbf{v}_{dqs4}^{e}$) as the hexagon shrinks. The voltage vector $\mathbf{v}_{dqs4}^{e}$ has a lower q-axis voltage component than that of $\mathbf{v}_{dqs1}^{e}$. It can be noticed from (7) that $\mathbf{v}_{dqs4}^{e}$ leads to the decreased d-axis current which causes a lower flux linkage at a given rotor speed. This suggests that an automatic field-weakening operation and maximum voltage utilization can be achieved simultaneously without requiring an extra control function. In addition, a rapid mode transition between MBC and HVC is possible without control manipulations because no integrators are involved for motor air-gap torque regulations. This feature is beneficial to small capacitor inverter applications that are subject to an unexpected grid voltage dip, frequent dc voltage fluctuation, and variable dc voltage ripples resulted from the grid-side impedance.

B. Compensation of Effects of Parameter Drifts

In practice, the rotor flux level is not maintained properly in the MBC and HVC modes because the machine parameters of

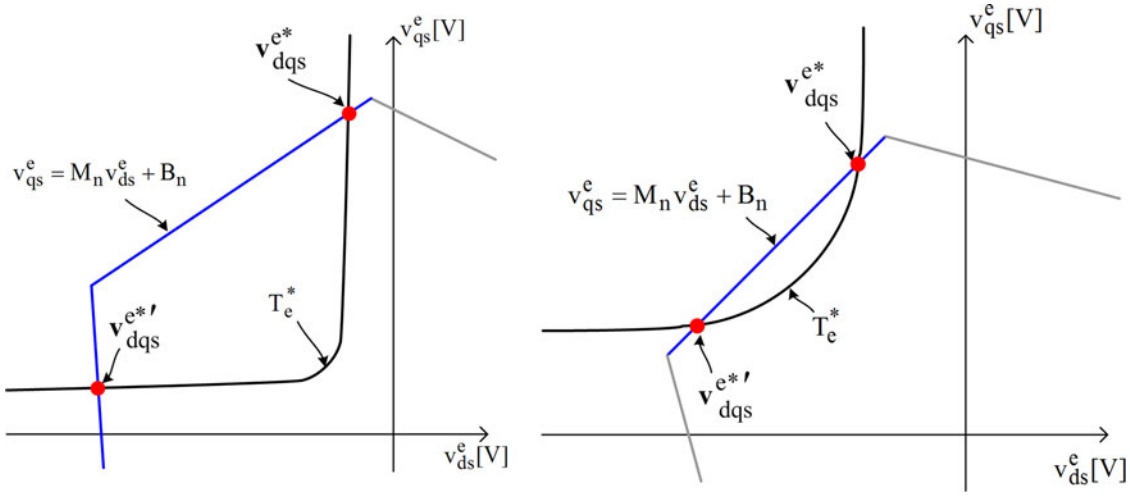

Fig. 5. Feasible voltage vector selection strategy.

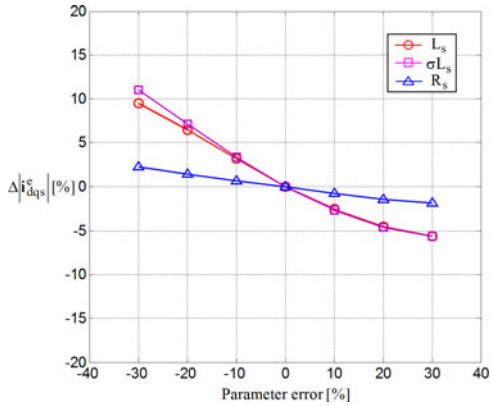

Fig. 6. Stator current deviation by motor parameter drifts at 0.6 p.u. of the rated speed.

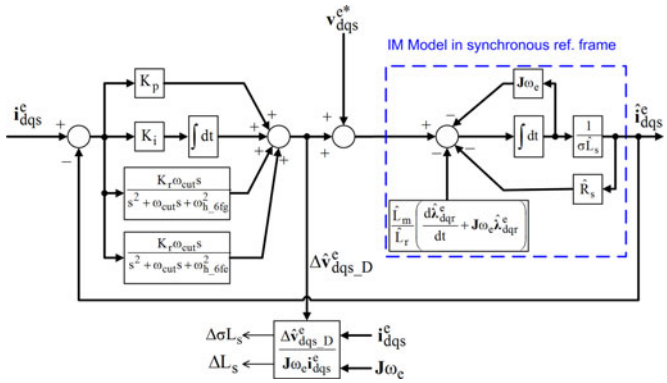

Fig. 7. State-filter design for decoupling the parameter dependence.

TABLE I
RATINGS AND KNOWN PARAMETERS OF THE IM UNDER TEST

Ratings and parameters	Value	Unit
Rated power output	1.5	kW
Rated voltage	220	V
Rated speed	1500	r/min
R_s / R_r at 25 °C	2.47 / 0.7	Ω
$L_m / \sigma L_s$	134 / 12.6	mH

(6a), (6b), (10a), and (10b) drift due to magnetic saturation and initial errors. The voltage errors of (6a), (6b), (10a), and (10b) also result in an incorrect actual stator current, which might result in high copper or iron losses for a given torque condition. In HVAC applications, the main operation is performed in the speed range from 50% up to 90% of the rated motor speed. Fig. 6 shows the stator current deviation trajectories of a tested IM, as shown in Table I, at 60% of the rated speed and 67% of the rated torque. The stator resistance error has little impact on the current deviation at this speed.

In practical applications, an online compensation for model errors is believed to be more effective in achieving accurate motor control. This paper proposes a voltage disturbance state-filter [14] to decouple the parameter dependence of MBC and HVC modes. Fig. 7 presents a block diagram of the disturbance voltage estimation strategy using a complex vector representation in the synchronous reference frame. A familiar PI-type Luenberger-style model-current observer controller was adopted to estimate the voltage disturbance resulting from parameter variations, where the estimated output current $\hat{\mathbf{i}}^{e}_{dqs}$ follows the stator current $\mathbf{i}^{e}_{dqs}$. Because the command voltage vector $\mathbf{v}^{e*}_{dqs}$ is fed-forward to the observer, the voltage disturbance error $\Delta\hat{\mathbf{v}}^{e}_{dqs\_D}$ can be estimated at the output of the observer controller. Here, the stator current has a certain amount of harmonics with six times the synchronous and grid frequency due to the manipulated voltage on the hexagon boundary and fluctuating dc-bus voltage. A resonant-type filter is introduced to reject these ripple components of $\mathbf{i}^{e}_{dqs}$, which achieves enormously high gains at resonant frequencies of concern. This structure can estimate and compensate for voltage deviation resulting from disturbances and uncertainties [14].

The estimated disturbance voltage and stator current in the s-domain are given by as (11) and (12) shown at the bottom of the page, where K_p and K_i represent the PI gains. ω_{h_6fg}, ω_{f_6fe}, $\omega_{\rm cut}$, and K_r represent the grid frequency, concerned synchronous frequency, 3-dB cut-off frequency, and resonant filter gain, respectively. In this paper, superscript "^" represents the corresponding variables are estimated.

Substituting (12) into (11) yields

$$TF_{ctr}(s)\Delta\hat{\mathbf{v}}^e_{dqs\_D} = (\hat{R}_s + s\sigma\hat{L}_s + \mathbf{J}\omega_e\sigma\hat{L}_s)\mathbf{i}^e_{dqs} + s\frac{\hat{L}_m}{\hat{L}_r}\hat{\lambda}^e_{dqr} + \mathbf{J}\frac{\hat{L}_m}{\hat{L}_r}\omega_e\hat{\lambda}^e_{dqr} - \mathbf{v}^{e*}_{dqs} \quad (13a)$$

where

$$TF_{ctr}(s) = 1 + \frac{\hat{R}_s + s\sigma\hat{L}_s + \mathbf{J}\omega_e\sigma\hat{L}_s}{\left(\frac{K_p s+K_i}{s} + \frac{K_r\omega_{\rm cut}s}{s^2+\omega_{\rm cut}s+\omega^2_{h\_6fg}} + \frac{K_r\omega_{\rm cut}s}{s^2+\omega_{\rm cut}s+\omega^2_{h\_6fe}}\right)}. \quad (13b)$$

At the steady-state (s→0), the estimated *d*–*q*-axis disturbance voltage can be obtained by substituting (1) into (13a)

$$\Delta\hat{v}^e_{ds\_D} = \Delta R_s i^e_{ds} - \omega_e\Delta\sigma L_s i^e_{qs} - \omega_e\left(\frac{\hat{L}_m}{\hat{L}_r}\hat{\lambda}^e_{qr} - \frac{L_m}{L_r}\lambda^e_{qr}\right)$$
$$\Delta\hat{v}^e_{qs\_D} = \Delta R_s i^e_{qs} + \omega_e\Delta\sigma L_s i^e_{ds} + \omega_e\left(\frac{\hat{L}_m}{\hat{L}_r}\hat{\lambda}^e_{dr} - \frac{L_m}{L_r}\lambda^e_{dr}\right) \quad (14)$$

where $\Delta R_s = \hat{R}_s - R_s$ and $\Delta\sigma L_s = \sigma\hat{L}_s - \sigma L_s$.

For the RFO IM, (14) can be rewritten as

$$\Delta\hat{v}^e_{ds\_D} = \Delta R_s i^e_{ds} - \omega_e\Delta\sigma L_s i^e_{qs}$$
$$\Delta\hat{v}^e_{qs\_D} = \Delta R_s i^e_{qs} + \omega_e\Delta L_s i^e_{ds} \quad (15)$$

where $\Delta L_s = \hat{L}_s - L_s$.

From (15), the inductance values used in (6a), (6b), (10a), and (10b) can be identified by neglecting the stator resistance voltage drop

$$\Delta\sigma L_s \cong -\frac{\Delta\hat{v}^e_{ds\_D}}{\omega_e i^e_{qs}}$$
$$\Delta L_s \cong \frac{\Delta\hat{v}^e_{qs\_D}}{\omega_e i^e_{ds}}. \quad (16)$$

Fig. 8 shows the simulated compensation results of the parameter variation effect at 60% of the base speed and 67% of the load torque. In Fig. 8(a), L_s was set to be +15% of its nominal value and (16) was delivered at $t = 1$ s. After 1 s, the deviation of the stator current and rotor flux linkage was reduced to almost zero. The same test was repeated at −15% of ΔL_s, as shown in Fig. 8(b). These test results indicate that the stator current and rotor flux linkage were controlled precisely against parameter mismatch because the proposed compensation method provides a concurrent estimation of the magnetic saturation and initial error. Therefore, this design can be effective in accurately estimating and compensating for the MBC and HVC modes while reducing the computational complexity. Fig. 9 presents an overall block diagram of the control system augmented to include the proposed algorithm to compensate for the parameter variation effects in real time. A simple back-EMF tracking-based position sensorless method was employed for a motor position estimation [15].

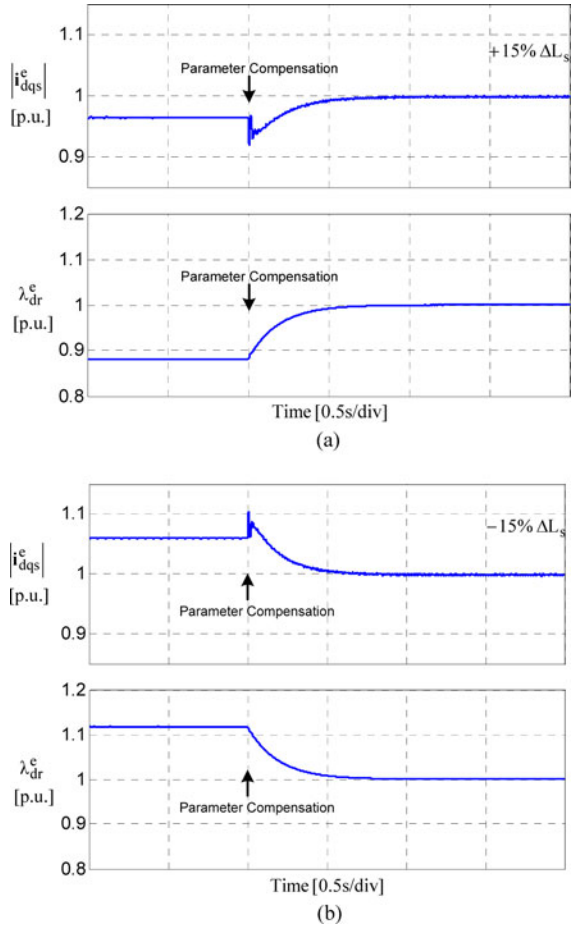

Fig. 8. Inductance compensation results. (a) +15% ΔL_s. (b) +15% ΔL_s.

$$\Delta\hat{\mathbf{v}}^e_{dqs\_D} = \left(\hat{R}_s\hat{\mathbf{i}}^e_{dqs} + s\sigma\hat{L}_s\hat{\mathbf{i}}^e_{dqs} + \mathbf{J}\omega_e\sigma\hat{L}_s\hat{\mathbf{i}}^e_{dqs} + s\frac{\hat{L}_m}{\hat{L}_r}\hat{\lambda}^e_{dqr} + \mathbf{J}\frac{\hat{L}_m}{\hat{L}_r}\omega_e\hat{\lambda}^e_{dqr}\right) - \mathbf{v}^{e*}_{dqs} \quad (11)$$

$$\hat{\mathbf{i}}^e_{dqs} = \mathbf{i}^e_{dqs} - \frac{1}{\left(\frac{K_p s+K_i}{s} + \frac{K_r\omega_{\rm cut}s}{s^2+\omega_{\rm cut}s+\omega^2_{h\_6fg}} + \frac{K_r\omega_{\rm cut}s}{s^2+\omega_{\rm cut}s+\omega^2_{h\_6fe}}\right)}\Delta\hat{\mathbf{v}}^e_{dqs\_D} \quad (12)$$

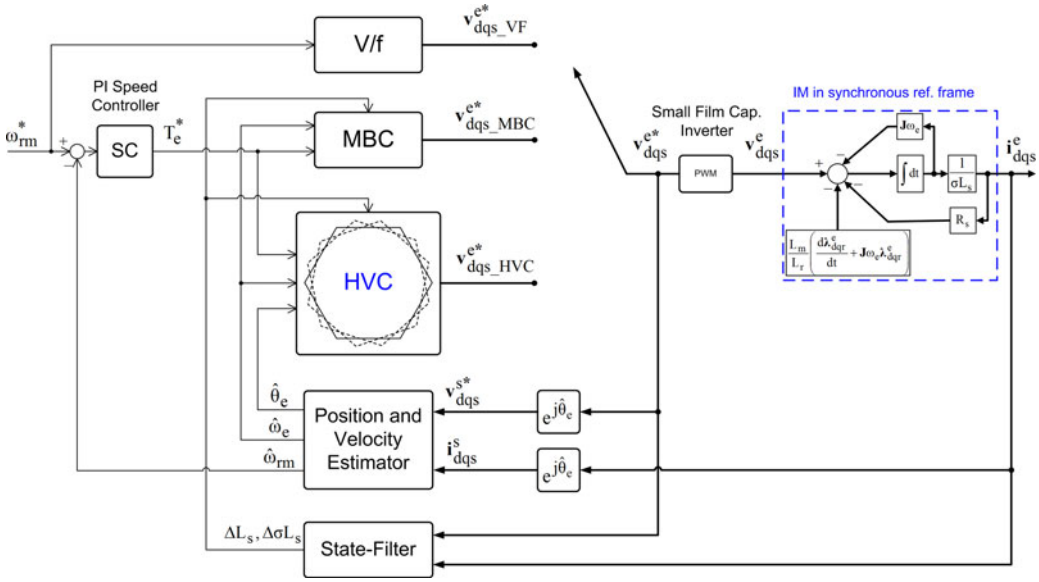

Fig. 9. Overall control block diagram.

III. Simulation and Experimental Results

Validation of the theoretical developments presented earlier was performed on a 1.5-kW IM drive with a 20-μF film capacitor fed by a three-phase diode rectifier through a simulation and real test.

A 4096 pulses-per-revolution encoder was mounted to one end of the IM to monitor the rotor speed. The other end of the shaft was coupled to a 1.5-kW dc generator to control the external load. The algorithm was implemented in the inverter with a constant PWM switching frequency of 5 kHz. The nominal input line-to-line voltage was set to 210 V and the advent of flux weakening occurs at approximately 1500 r/min. The online disturbance state-filter was performed every 100 μs and the bandwidth of the state-filter and PI speed controller was set to 600 rad/s. The gain (K_r) of the resonant controller and 3-dB cut-off frequency ($\omega_{\rm cut}$) are fixed to 3 and 50 Hz, respectively. In all experimental tests, the running conditions were identical to those in the simulation.

Fig. 10 presents a simulated result in the motoring operation, where the dc-link voltage, flag signal, air-gap torque, and rotor flux linkage are illustrated from top to bottom. The "mode_HVC" is 1 if the HVC mode activates and 0 otherwise (MBC mode). In this test, the IM drive was operated with 90% of the base speed while the rated load torque was applied. The dc-link voltage fluctuates with six times the input grid voltage frequency. The waveform of the flag signal and air-gap torque show a smooth and rapid transition occurs between the MBC and HVC operation. This is because the proposed MBC and HVC were designed without integrators for current control and with the same voltage selection rule. This structure leads to a single control law in the entire operating region, which avoids secondary upsets by the control mode switching and complexity of having an additional control function or gain to be adjusted.

Fig. 11 shows the experimental results in the same test scenario, where the measured dc-link voltage, flag signal, estimated

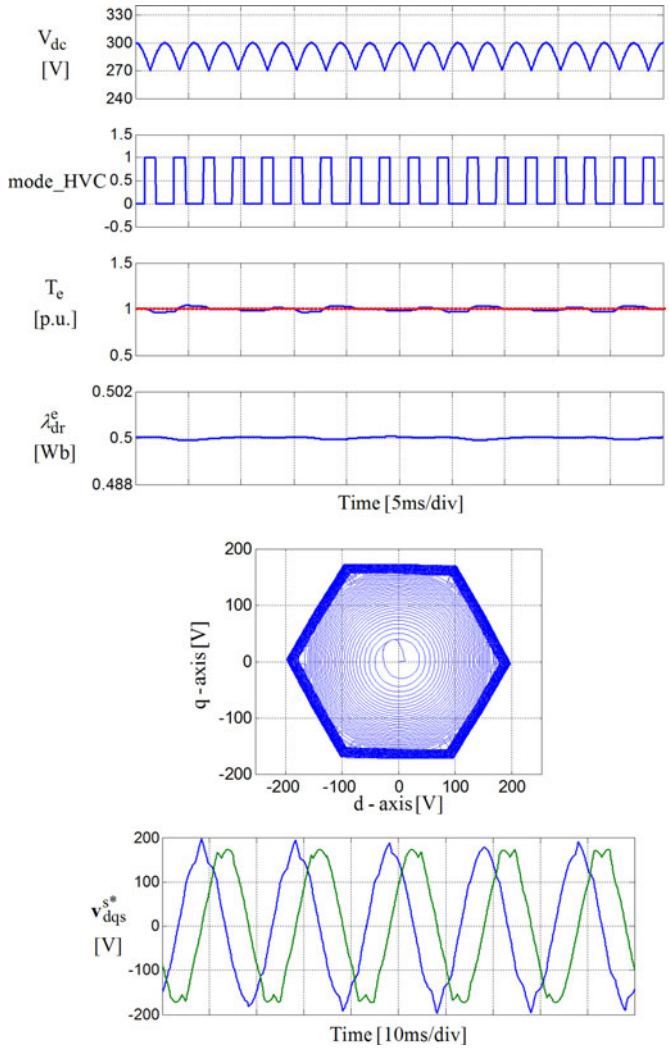

Fig. 10. Simulated results of the proposed control method.

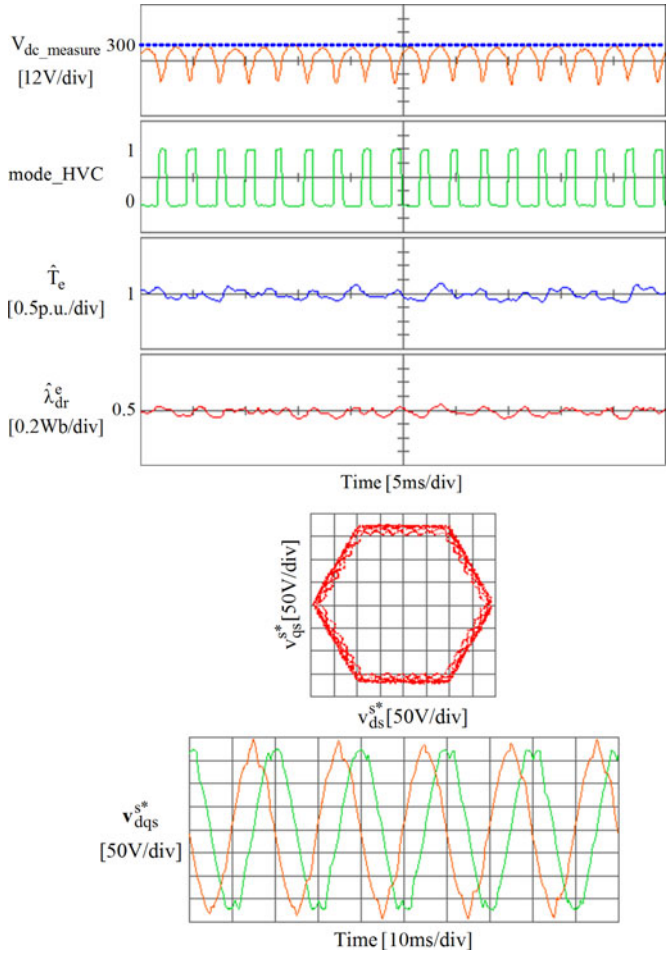

Fig. 11. Test results of the proposed control method.

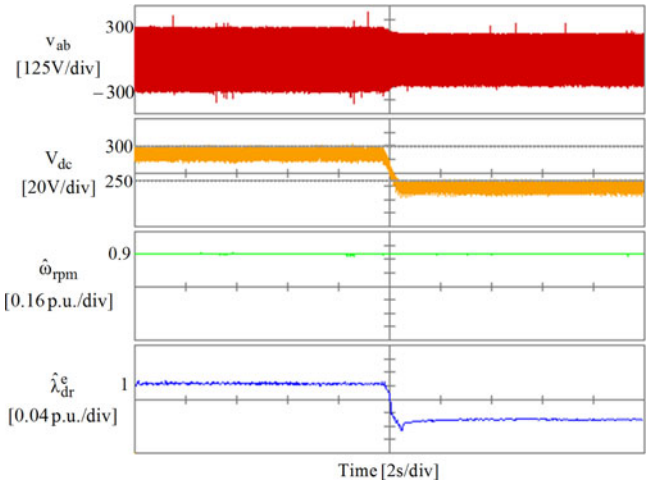

Fig. 12. HVMC operation during the grid voltage transients.

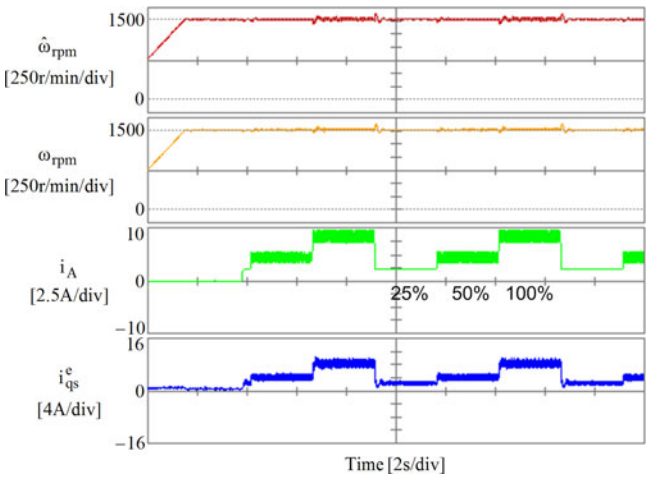

Fig. 13. Load test result of the proposed method.

air-gap torque, and estimated rotor flux linkage are, respectively, illustrated from top to bottom. The desired torque was well regulated with the average value because the proposed state-filter provides a concurrent compensation. Although a sufficient control voltage margin is essential to the current regulator-based strategy for feedback corrections, the proposed method is immune to a lack of available voltage because it manipulates the output voltage instead of controlling the motor current. A close match was observed between simulation and test result. The x–y locus shows that the resulting controller can achieve the maximum voltage utilization at the periodic voltage dropping region.

Particular attention should be paid to the field-weakening operation of the proposed HVC mode because a sudden grid voltage drop forces the drive to enter the field-weakening region. Fig. 12 shows the field-weakening operation results, where the three-phase source voltage suddenly drops by 15% of its nominal value at 90% of the rated speed.

The line-to-line grid voltage, measured dc-bus voltage, the estimated rotor velocity, and rotor flux linkage are depicted from top to bottom. In the waveform of the dc-bus voltage and the rotor flux, it can be noticed that an automatic and rapid transition occurs between nonlimited operation and field-weakening mode without any subcontrol functions used in the current control strategy. This feature is beneficial for achieving the ability to maintain the inverter operation during the grid voltage transients.

Fig. 13 shows the test result at the base speed, whereas the external load was increased stepwise from 0% to the rated value. This load torque test can be thought to be as being more severe than would be encountered in practical situations. The estimated/controlled rotor speed, actual rotor speed for monitoring, measured armature current of the dc generator, and q-axis stator current of the tested IM are illustrated from top to bottom. Distortions were rarely found during the velocity transition of each control mode. The drive does not lose its control capability in the presence of the full load torque, which means that the motor generates the desired air-gap torque with reasonable accuracy that is comparable to that of commercial ac drive systems. With the proposed algorithm, the inverter requirements of a long lifetime, high reliability, and high power density can be achieved without sacrificing the system performance.

IV. Conclusion

This paper addresses the controller design of a position sensorless vector-controlled IM drive system supplied from a small dc-link film capacitor inverter fed by a three-phase diode front-end rectifier. The proposed approach focuses on the controller performance when entering or leaving the infeasible voltage domain. The PI motor-current-regulator-free control structure presents a smooth transition from the MBC under the unconstrained voltage region to the HVC when the voltage limit is encountered. The analytical solution leads to the dynamic voltage modification at each time step with respect to the available dc-bus voltage. The algorithm can provide adequate results over a number of potential secondary upsets found in the current regulator-based control structure. The operation sensitivity under motor parameter drifts is also examined to decouple its influence using a voltage disturbance state filter. The test results clearly show that the proposed method can improve the inverter reliability without sacrificing the motor control performance.

References

[1] *Altivar 21 User's Manual,* Schneider Electric Industries S.A.S., Rueil Malmaison, France, 2006.

[2] K. W. Lee, M. Kim, J. Yoon, S. B. Lee, and J. Y. Yoo, "Condition monitoring of dc-link electrolytic capacitors in adjustable-speed drives," *IEEE Trans. Ind. Appl.*, vol. 44, no. 5, pp. 1606–1613, Sep./Oct. 2008.

[3] M. L. Gasperi, "Life prediction modeling of bus capacitors in AC variable frequency drives," *IEEE Trans. Ind. Appl.*, vol. 41, no. 6, pp. 1430–1435, Nov./Dec. 2005.

[4] A. Layhani, P. Venet, G. Grellet, and P. J. Viverge, "Failure prediction of electrolytic capacitors during operation of a switchmode power supply," *IEEE Trans. Power Electron.*, vol. 13, no. 6, pp. 1199–1207, Nov. 1998.

[5] A. M. Imam, T. G. Habetler, R. G. Harley, and D. M. Divan, "Real-time condition monitoring of the electrolytic capacitors for power electronics applications," in *Proc. IEEE Appl. Power Electron. Conf.*, 2007, pp. 1057–1061.

[6] D. C. Lee, J. K. Seok, and J. W. Choi, "Online capacitance estimation of DC-link electrolytic capacitors for three-phase AC/DC/AC PWM converters using recursive least squares method," *Proc. Inst. Electr. Eng.—Electr. Power Appl.*, vol. 152, no. 6, pp. 1503–1508, Nov. 2005.

[7] L. Malesani, L. Rossetto, P. Tenti, and P. Tomasin, "AC/DC/AC PWM converter with reduced energy storage in the DC link," *IEEE Trans. Ind. Appl.*, vol. 31, no. 2, pp. 287–292, Mar./Apr. 1995.

[8] A. Yoo, S. K. Sul, H. Kim, and K. S. Kim, "Flux-weakening strategy of an induction machine driven by an electrolytic-capacitor-less inverter," *IEEE Trans. Ind. Appl.*, vol. 47, no. 3, pp. 1328–1336, May/Jun. 2011.

[9] K. Inazuma, H. Utsugi, K. Ohishi, and H. Haga, "High-power-factor single-phase diode rectifier driven by repetitively controlled IPM motor," *IEEE Trans. Ind. Electron.*, vol. 60, no. 10, pp. 4427–4437, Oct. 2013.

[10] H. S. Jung, S. J. Chee, S. K. Sul, Y. J. Park, H. S. Park, and W. K. Kim, "Control of three phase inverter for AC motor drive with small DC-link capacitor fed by single phase AC source," in *Proc. IEEE Energy Convers. Congr. Expo. Conf.*, 2012, pp. 2985–2991.

[11] W. J. Lee, Y. Son, and J. I. Ha, "Single-phase active power filtering method using diode-rectifier-fed motor drive," in *Proc. IEEE Energy Convers. Congr. Expo. Conf.*, 2013, pp. 2461–2465.

[12] C. H. Choi, J. K. Seok, and R. D. Lorenz, "Wide-speed direct torque and flux control for interior PM synchronous motors operating at voltage and current limits," *IEEE Trans. Ind. Appl.*, vol. 49, no. 1, pp. 109–117, Jan./Feb. 2013.

[13] S. H. Kim and J. K. Seok, "Finite-settling steps direct torque and flux control (FSS-DTFC) for torque-controlled interior PM motors at voltage limits," *IEEE Trans. Ind. Appl.*, vol. 50, no. 5, Sep./Oct., 2014.

[14] S. H. Kim, C. H. Choi, and J. K. Seok, "Voltage disturbance state-filter design for precise torque-controlled interior permanent magnet synchronous motors," in *Proc. IEEE Energy Convers. Congr. Expo. Conf.*, 2011, pp. 2445–2451.

[15] H. Kim, M. C. Harke, and R. D. Lorenz, "Sensorless control of interior permanent-magnet machine drives with zero-phase lag position estimation," *IEEE Trans. Ind. Appl.*, vol. 39, no. 6, pp. 1726–1733, Nov./Dec. 2003.

SeHwan Kim (S'10) received the B.S. degree from Yeungnam University, Gyeongsan, Korea, in 2010, where he is currently working toward the combined M.S./Ph.D. degree in the Power Conversion Laboratory.

His current research interests include high performance electrical machine drives, battery voltage maximum utilization for EVs/HEVs, and precise torque control of PM synchronous motors.

Jul-Ki Seok (S'94–M'98–SM'09) received the B.S., M.S., and Ph.D. degrees from Seoul National University, Seoul, Korea, in 1992, 1994, and 1998, respectively, all in electrical engineering.

From 1998 to 2001, he was a Senior Engineer with the Production Engineering Center, Samsung Electronics, Suwon, Korea. Since 2001, he has been a member of the faculty of the School of Electrical Engineering, Yeungnam University, Gyeongsan, Korea, where he is currently a Professor. His specific research areas are motor drives, power converter control of offshore wind farms, and nonlinear system identification related to the power electronics field.

Dr. Seok serves as an Associate Editor of the IEEE Transactions on Industry Applications.